nature physics

ARTICLES

https://doi.org/10.1038/s41567-022-01653-5

Check for updates

Time-reversal-based quantum metrology with many-body entangled states

Simone Colombo[1,4], Edwin Pedrozo-Peñafiel[1,4], Albert F. Adiyatullin[1,3,4], Zeyang Li[1], Enrique Mendez[1], Chi Shu[1,2] and Vladan Vuletić[1]✉

Linear quantum measurements with independent particles are bounded by the standard quantum limit, which limits the precision achievable in estimating unknown phase parameters. The standard quantum limit can be overcome by entangling the particles, but the sensitivity is often limited by the final state readout, especially for complex entangled many-body states with non-Gaussian probability distributions. Here, by implementing an effective time-reversal protocol in an optically engineered many-body spin Hamiltonian, we demonstrate a quantum measurement with non-Gaussian states with performance beyond the limit of the readout scheme. This signal amplification through a time-reversed interaction achieves the greatest phase sensitivity improvement beyond the standard quantum limit demonstrated to date in any full Ramsey interferometer. These results open the field of robust time-reversal-based measurement protocols offering precision not too far from the Heisenberg limit. Potential applications include quantum sensors that operate at finite bandwidth, and the principle we demonstrate may also advance areas such as quantum engineering, quantum measurements and the search for new physics using optical-transition atomic clocks.

Over the last two decades, substantial effort has been devoted towards the design of protocols and the engineering of quantum states that enable the operation of atomic sensors beyond the standard quantum limit (SQL)[1–18]. The SQL arises from the discreteness of outcomes in the quantum measurement process, that is, the quantum projection noise, and sets the limit of precision of $1/\sqrt{N}$ that can be achieved with a system of N independent particles. The SQL can be overcome by generating many-body entanglement, which is most commonly achieved by means of spin squeezing[19–22], where a state of the collective spin with reduced quantum noise along one quadrature is created and detected. Such an approach is often limited by the precision of the readout rather than the generation of the squeezed state[2,8,9,12].

The ultimate boundary for linear quantum measurements is the Heisenberg limit (HL), where the precision improves with the particle number as $1/N$. The HL can be reached with maximally entangled states, or equivalently, when the quantum Fisher information F of the system is the largest[23]. Maximally entangled states at a fidelity exceeding the classical limit of 0.5 have been generated in systems of up to 24 particles[16–18,24], but they are challenging to create and maintain in many-atom systems that are of interest for metrological applications. As an alternative, more easily implementable schemes and quantum states where the precision improves as b/N (Heisenberg scaling, HS[25–27]), at fixed distance $b \geq 1$ from the HL, have been identified. One such approach is to create an entangled state with a large quantum Fisher information via a Hamiltonian process, then subject the system to the signal to be measured (that is, a phase shift φ) before evolving it 'backwards in time' by applying the negative Hamiltonian. This Loschmidt echo-like approach[26–31] results in a final state that is displaced relative to the initial state and where, under appropriate conditions, the phase signal of interest φ has been effectively amplified. Such signal amplification using a time-reversed interaction (SATIN) protocol can make use of complex states with large quantum Fisher information, which are not necessarily simple squeezed states with a Gaussian envelope, and can potentially provide HS and a sensitivity quite close to the HL even at the limited resolution of the final measurement[26,27,30].

Previously, non-Gaussian many-body entangled states have been generated experimentally in Bose–Einstein condensates[32,33], neutral cold atoms[34] and cold trapped ions[11], while time-reversal-type protocols have been implemented using phase shifts in a three-level system for a few neutral atoms[35] or using the coupling to a motional mode in combination with spin rotations for ~150 trapped ions[36]. Experiments demonstrating HS have also been performed, albeit either using squeezed spin states and therefore being limited far (>46 dB) from the HL[37] or involving a relatively small number ($N \leq 20$) of atoms[17,18,24]. Furthermore, amplification of the quantum phase in a neutral atom system coupled to an optical resonator has been demonstrated through a protocol interspersing spin squeezing with a state rotation. Remarkably, this has enabled the detection of −8 dB noise reduction without the need for a detection resolution below the SQL[10]. This protocol has been performed in, and requires, a regime where the collective states live on a flat phase space and hence can only operate far from the HL.

Here, following the SATIN protocol proposed in ref. [26], we create a highly non-Gaussian entangled state in a system of ^{171}Yb atoms and demonstrate phase sensitivity with HS (b/N) at a fixed distance $b = 12.6$ dB from the HL. When used in a Ramsey sequence in an atomic interferometer, we achieve the highest metrological gain over the SQL, $\mathcal{G} = 11.8 \pm 0.5$ dB, that has been achieved in any (full Ramsey) interferometer to date. The demonstrated SATIN protocol can be readily applied to state-of-the-art optical lattice clocks by mapping the generated entangled state onto the optical clock transition via a coherent optical π-pulse[14]. It is worth noting that, to avoid large systematic errors due to collisions, optical lattice clocks[38]

[1]Department of Physics, MIT-Harvard Center for Ultracold Atoms and Research Laboratory of Electronics, Massachusetts Institute of Technology, Cambridge, Massachusetts, USA. [2]Department of Physics, Harvard University, Cambridge, Massachusetts, USA. [3]Present address: Laboratoire PhLAM, Université de Lille, Lille, France. [4]These authors contributed equally: Simone Colombo, Edwin Pedrozo-Peñafiel, Albert F. Adiyatullin. ✉e-mail: vuletic@mit.edu

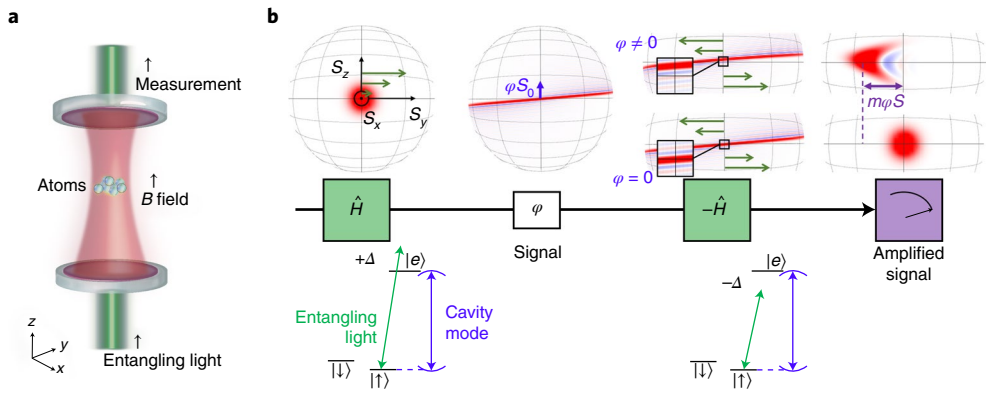

Fig. 1 | Setup and sequence. a,[171]Yb atoms are trapped inside an optical cavity in an optical lattice (red light beam). Light for state preparation, entanglement generation and state measurement (green) is sent through the cavity along the *z* axis. The static magnetic field defines the quantization axis parallel to *z*. **b**, The SATIN protocol sequence with the quantum state evolution (top) and relevant energy levels and cavity mode (bottom). The Wigner quasi-probability distribution functions describing the collective quantum state are calculated for an ensemble of 220 atoms, and are represented on the generalized Bloch sphere for the ground-state manifold $\{|\downarrow\rangle, |\uparrow\rangle\}$. An entangling light pulse is passed through the cavity, detuned by $+\Delta$ from the $|\uparrow\rangle \rightarrow |e\rangle$ transition and the cavity mode. This light generates the nonlinear OAT Hamiltonian $\hat{H} \propto \hat{S}_z^2$ which shears the initial CSS state (green arrows on the generalized Bloch sphere). The state depicted here corresponds to a shearing angle of $\tilde{Q} = 0.7$. A rotation φ about the S_y axis displaces the state such that $\langle \hat{S}_z \rangle = \varphi S_0$. This rotation can be induced both by a direct resonant RF pulse or effectively via a compound sequence $\mathcal{R}_y(\pi/2)\mathcal{R}_z(\varphi)\mathcal{R}_y(-\pi/2)$ as in Ramsey spectroscopy with squeezed states (where $\mathcal{R}_j(\alpha)$ denotes a rotation by an angle α about the *j* axis). We first characterize the protocol by applying a direct rotation along the *y* axis, while later we implement it in a phase-sensitive Ramsey sequence, where the $\mathcal{R}_z(\varphi)$ results from the accumulated phase in a spin echo sequence. Subsequently, a (dis)entangling light pulse is sent through the cavity, detuned by $-\Delta$ from the $|\uparrow\rangle \rightarrow |e\rangle$ transition and the cavity mode. This pulse generate the negative OAT Hamiltonian $-\hat{H}$ which causes the quantum state to evolve effectively 'backwards in time'. With $\varphi = 0$ the quantum state evolves back to the original CSS, while for a small angle ($\varphi \neq 0$) the final state is displaced by an angle $m\varphi$ from the original CSS, where *m* is the SATIN signal amplification. At every shot, we measure the total atom number *N* (Methods).

operate with a limited total atom number of $N = 10^2$–10^4, a regime that we reach and investigate here with the SATIN protocol.

Our system consists of up to $N = 400$ laser-cooled ^{171}Yb atoms that are trapped in an optical lattice inside a high-finesse optical resonator (Fig. 1a)[12]. We work in the nuclear spin manifold $s = \frac{1}{2}$ of the electronic ground state $^1S_0$ and first create a state with the collective atomic spin $\hat{\mathbf{S}} = \sum \hat{\mathbf{s}}_i$ pointing along the *x* axis (a coherent spin state, CSS). The collective spin operators are defined through the Pauli matrices ($\hat{\sigma}_{x,y,z}$) as $\hat{S}_k = (1/2)\sum_{j=1}^{N} \hat{\sigma}_{k,j}$ with $k = x, y, z$. In this product state of the individual spins $\mathbf{s}_i$, each atom is in a superposition of the states $|\uparrow\rangle \equiv \left|m_s = +\frac{1}{2}\right\rangle$ and $|\downarrow\rangle \equiv \left|m_s = -\frac{1}{2}\right\rangle$. We then apply the one-axis twisting (OAT) Hamiltonian[20]

$$\hat{H} = \chi \hat{S}_z^2 \tag{1}$$

to the CSS to create an entangled state (Fig. 1). The OAT Hamiltonian is generated by the nonlinear interaction between the atoms and the light that is being applied to the cavity[12,14] (Methods). The light–atom interaction as a generator of entanglement offers the advantage that not only can it be turned on or off arbitrarily but also that the sign of $\hat{H}$ can be changed by adjusting the frequency of the incident light (Methods). When we apply $\hat{H}$ for a time *t*, the state evolves under the OAT operator $\hat{U} = \exp\left(-\mathrm{i}\frac{\tilde{Q}}{\sqrt{N}}\hat{S}_z^2\right)$, where we have introduced the normalized twisting parameter $\tilde{Q} \equiv \sqrt{N}\chi t$. (Here, $\tilde{Q} = 2\pi$ would correspond to a state wrapped all around the Bloch sphere.)

We first characterize the action of the OAT Hamiltonian $\hat{H}$ and the effective evolution 'backwards in time' that can be obtained by applying $-\hat{H}$ subsequently to $\hat{H}$. To this end, we measure for various twisting strengths $\tilde{Q}_+$ the spin distribution along the S_y axis and its normalized variance $\sigma_y^2 \equiv 2(\Delta S_y)^2/S_0$. (Here, $S_0 = N/2$ and the SQL, obtained for the CSS, corresponds to $\sigma_y^2 = 1$.) For small $\tilde{Q}_+ \ll 1$, the OAT operator $\hat{U}(\tilde{Q}_+)$ creates an squeezed spin state with a Gaussian envelope, while for $\tilde{Q}_+ \geq 0.5$, the state stretches around a substantial portion of the Bloch sphere. As Fig. 2a shows, we observe strongly non-Gaussian probability distributions along the S_y axis that agree well with the expected evolution from the OAT Hamiltonian calculated without any free parameters (Methods). We also verify that the $\hat{S}_z$ distribution remains unaffected by the OAT.

If we subsequently apply the negative Hamiltonian and the corresponding untwisting operator $\hat{U}(\tilde{Q}_-)$, then for a matched untwisting magnitude, $\tilde{Q}_- = -\tilde{Q}_+$, the state distribution for the S_y axis reverts back to a Gaussian distribution with a variance that is only slightly increased compared with the original CSS (Fig. 2a, bottom and Fig. 2b). The residual broadening can be explained by the fact that the OAT Hamiltonian $\hat{H}$ of equation (1) is only an approximation to the actual physical process, where the transmitted and scattered light carries some residual information about the atomic spin $\hat{S}_z$. Then, tracing over the unobserved light degrees of freedom causes an excess broadening of σ_y^2 by a factor $1 + \mathcal{I}$ (ref. [12]). To quantify the excess broadening $\mathcal{I}$, we fix $\tilde{Q}_+$ and measure σ_y^2 versus $\tilde{Q}_-$. Data for $\tilde{Q}_+ = 0.5$ and $N = 220$ atoms in average are shown in Fig. 2b. It is clear that σ_y^2 is indeed minimized near $\tilde{Q}_- = -\tilde{Q}_+$, with a small excess broadening of $\mathcal{I} = 0.9 \pm 0.4 \lesssim 1$, comparable to the initial noise area of the CSS (1 in the chosen units), after accounting for the measurement resolution (increasing σ_y^2 by 0.15 ± 0.02) and contrast loss (decreasing σ_y^2 by 0.7 ± 0.1). Our algebraic model, without any fitting parameters, agrees remarkably well with the data. Figure 2c shows the variance of $\hat{S}_y$ resulting from the shearing $\tilde{Q}_+$ (solid circles) and after the unshearing $\tilde{Q}_-$ (open circles). The data points are fitted to the theoretical curve taking into account the different sources of decoherence: the excess broadening $\mathcal{I}$, the finite contrast $\mathcal{C}$ and the measurement resolution σ_{meas}^2.

We next measure the small-signal amplification *m* provided by the SATIN protocol. To this end, we prepare a strongly entangled state by evolving a CSS under the OAT operator $\hat{U}(\tilde{Q}_+)$, rotate this state by a small angle φ around the *y* axis such that $\langle \hat{S}_z \rangle = \varphi S_0$ (where $\langle \cdot \rangle$ represents the expectation value of the operators) and apply the untwisting operator $\hat{U}(\tilde{Q}_- = -\tilde{Q}_+)$ which amplifies φ by a factor *m* and maps it onto the *y* axis, resulting in $\langle \hat{S}_y \rangle = m\varphi S_0$. We measure

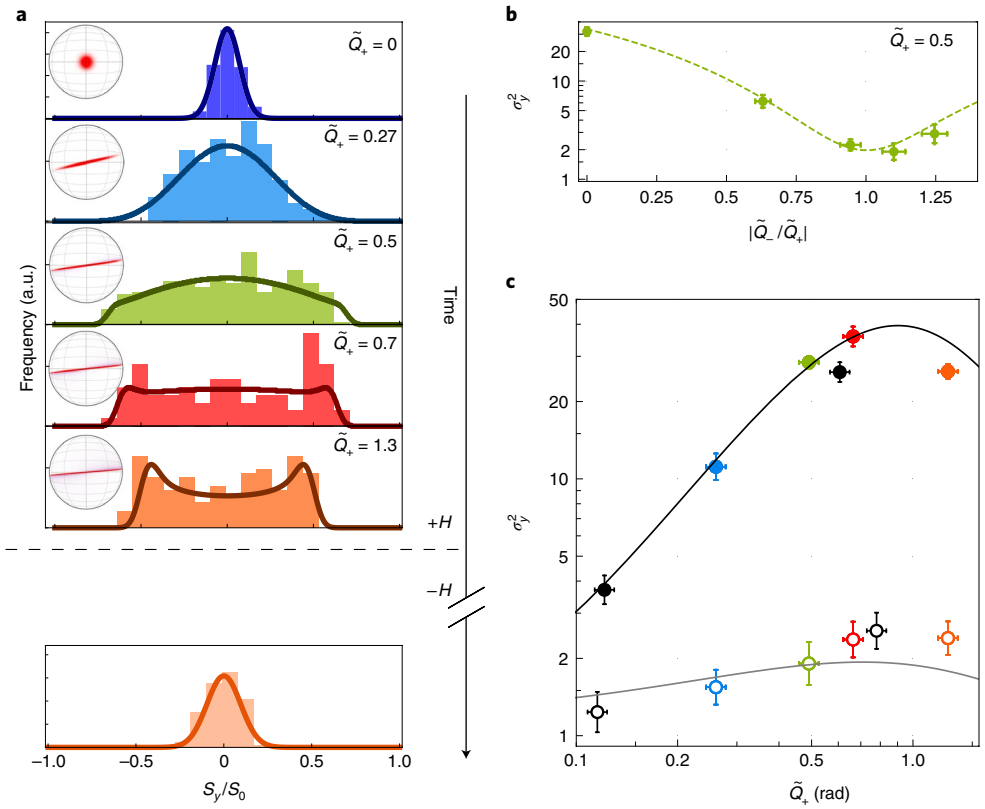

Fig. 2 | The state evolution during the SATIN sequence. a, Histograms showing the distributions along the S_y axis measured at different times during the SATIN sequence. The system transitions from Gaussian states (blue) to strongly non-Gaussian states (red and orange). After reversing the sign of the Hamiltonian, the original CSS is almost recovered (orange, lower plot). The solid lines are the distributions predicted by a theoretical model including a finite contrast of $\mathcal{C}$, a measurement resolution of $\sigma^2_{\mathrm{meas}} = 0.15$ (that is, a resolution of 6 atoms for $N = 220$) and an excess broadening from light–atom entanglement of $\mathcal{I}$. The Bloch spheres show the expected Wigner quasi-probability distributions at the corresponding times. **b**, The normalized S_y variance ($\sigma_y^2 \equiv 2(\Delta S_y)^2/S_0$) as a function of the unshearing strength $\tilde{Q}_-$ for $\tilde{Q}_+ = 0.5$. The dashed line shows the model prediction. **c**, Measured variances of S_y resulting from shearing with $\tilde{Q}_+$ (filled circles) and after the corresponding unshearing $\tilde{Q}_-$ (open circles), with $\tilde{Q}_- = -\tilde{Q}_+$. The solid lines are theoretical predictions, including $\mathcal{C}$, σ^2_{meas} and $\mathcal{I}$. All error bars represent the 1σ statistical uncertainty resulting from 100–150 experimental realizations. The error bars for σ_y^2 are inferred by bootstrapping the data.

how $\langle \hat{S}_y \rangle / S_0$ scales with φ for different $\tilde{Q}_+$ and present the results in Fig. 3a, which compares the signal amplification of the SATIN scheme versus a measurement with a CSS (for which $m_{\mathrm{SQL}} = 1$). Note that, for large displacements φ, the finite size of the Bloch sphere makes the mapping of the rotation angle φ onto $\langle \hat{S}_y \rangle$ nonlinear. The measured data are well described by the model (Methods). Figure 3b shows the amplification m versus $\tilde{Q}_+$ together with the theoretical model. The amplification scales linearly with $\tilde{Q}_+$ for $\tilde{Q}_+ \ll 1$ and reaches its maximum at $\tilde{Q}_+ \approx 0.7$, larger than the optimum value of $\tilde{Q}_+ = 0.4$ for minimizing the variance of the spin squeezed state for the same atom number[12]. Even the state with $\tilde{Q}_+ = 1.3$ outperforms the squeezed state by several decibels. This non-Gaussian state has a root mean squared (r.m.s.) phase spread of 1.3 rad, where a state with a uniform distribution between 0 and 2π would have an r.m.s. phase spread of $\pi/\sqrt{3} \approx 1.8$ rad. This demonstrates the usefulness of non-Gaussian states for quantum metrology.

The sensitivity $\delta\varphi$ of the SATIN protocol, that is, the minimal resolvable displacement of a state, can be estimated as the displacement $mS_0\delta\varphi$ at the end of the sequence, which equals the measured uncertainty $\Delta S_y = \sigma_y\sqrt{S_0/2}$ after the twisting–untwisting sequence for $\varphi = 0$. Thus, the gain of the SATIN protocol over the SQL with sensitivity $(\Delta\varphi)_{\mathrm{SQL}} = 1/\sqrt{2S_0}$ is given by

$$\mathcal{G} = \frac{(\Delta\varphi)^2_{\mathrm{SQL}}}{(\delta\varphi)^2} = \frac{m^2}{\sigma_y^2} = \frac{S_0}{2}\frac{m^2}{(\Delta S_y)^2}. \qquad (2)$$

Figure 3c presents the resulting metrological gain $\mathcal{G}(\tilde{Q}_+)$ for an ensemble of $N = 220$ atoms. Since σ_y^2 does not change appreciably when increasing $\tilde{Q}_+$, the metrological gain approximately follows the behaviour of m and peaks at around $\tilde{Q}_+ \approx 0.7$. At larger values of $\tilde{Q}_+$, the signal amplitude is reduced due to contrast loss from photon scattering into free space. For $N = 220$ atoms, the metrological gain peaks at $\mathcal{G} = 10.8 \pm 0.6$ dB. This is more than 6 dB larger than the maximal gain achievable with spin squeezing in the same system, which is limited by the measurement resolution and decoherence to 4.7 dB.

Furthermore, we investigate the scaling of the sensitivity with the atom number N. Unlike spin squeezing[20] and the quantum magnification protocol of ref. [10], the SATIN protocol is not limited by the curvature of the Bloch sphere. Therefore we expect that, under optimum conditions, the precision will improve in proportion to the atom number, corresponding to HS. Figure 4 shows that, when we vary N between 50 and 370, we indeed measure a gain over the SQL that varies as $\mathcal{G} \propto N$, achieving HS. This implies that the averaging time necessary to achieve a certain resolution improves as N^2 for the SATIN protocol, as predicted in ref. [26]. In particular, for an average $N = 370$ atoms, we reach $\mathcal{G} = 12.8 \pm 0.9$ dB.

Finally, we implement a full (phase) interferometer for a.c. magnetic fields in the form of a spin echo SATIN Ramsey sequence. We first apply the OAT operator, then rotate the oversqueezed state about the S_x axis with a $\pi/2$ pulse, thus making it sensitive to phase

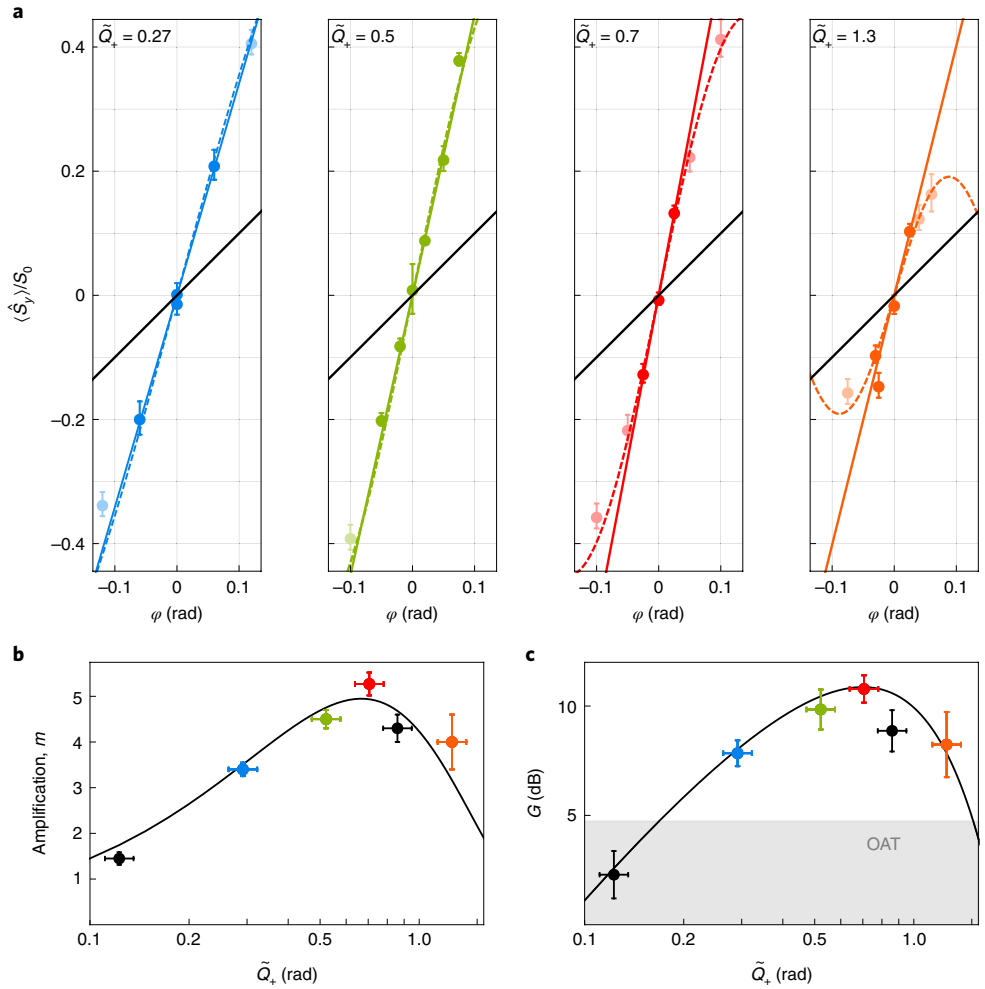

Fig. 3 | Signal amplification and metrological gain. a, The mean value $\langle \hat{S}_y \rangle / S_0$ as a function of the angle φ. The solid black line shows the maximal signal that can be reached with a CSS. The dashed coloured line represents the calculations, while the solid coloured line is a linear fit to the data for small φ. **b**, The signal amplification as a function of the shearing parameter $\tilde{Q}_+$. The solid line is the model prediction. **c**, The resulting metrological gain $\mathcal{G}$ as a function of the squeezing strength $\tilde{Q}_+$ with the model prediction (solid line). The grey area represents the metrological gain accessible with simple OAT squeezing in the same system with a measurement resolution of $\sigma^2_{\mathrm{meas}} = 0.15$ in variance (−8.2 dB). Coloured data points in **b** and **c** are obtained from the plots in **a**; same colour corresponds to same shearing parameter. Error bars represent 1σ confidence intervals. All data are taken with $208 \leq N \leq 232$ atoms. During each experimental repetition, the total atom number N is measured within an uncertainty of four atoms.

perturbations (that is, rotations about the S_z axis). Subsequently, we rotate the state back by applying another $\pi/2$ pulse about the S_x axis before subjecting it to the negative Hamiltonian. To cancel the fluctuations of the static magnetic field, we apply a spin echo π pulse, separated from the $\pi/2$ pulses by 1.73 ms, thus realizing an interferometer sensitive to a.c. magnetic fields with peak sensitivity at 290 Hz. We observe a metrological gain of $\mathcal{G} = 11.8 \pm 0.5$ dB with $N = 340 \pm 20$ atoms in the interferometer (Fig. 4c, solid red star), slightly exceeding the previous record of 10.5 ± 0.3 dB (ref. [9]) in a Ramsey interferometer (atomic clock) with large atom number. The gain $\mathcal{G}$ achieved with the SATIN Ramsey sequence represents a reduction by a factor of 15 in the averaging time for a desired precision (Fig. 4b). Our Ramsey interferometer also performs near the HS limit for the SATIN protocol (Fig. 4c, solid red star).

Under ideal conditions, the SATIN protocol provides a metrological gain that is only 4.3 dB away from the HL[26] for an optimized shearing strength of $\tilde{Q}_+^{\mathrm{opt}} = 1$. Dissipation in the atomic system, in our system due to photon scattering and light–atom entanglement, reduces the maximum available gain and the optimum shearing parameter $\tilde{Q}_+^{\mathrm{opt}}$. For our parameters, $\tilde{Q}_+^{\mathrm{opt}} = 0.7$, which reduces the metrological gain by 0.9 dB, while the interferometer contrast loss and non-unitary state evolution under the full Hamiltonian contribute 4.4 and 3.2 dB, respectively. The joint effect of these imperfections imposes a distance of 12.6 dB from the HL. To move closer to the HL, the dissipation in the system must be reduced by increasing the atom–cavity coupling, as characterized by the single-atom cooperativity η (Methods). For example, by increasing η by a factor of 10 to $\eta = 80$, we expect performance only 8 dB away from the HL. At present, we have seen no deviation from HS. That is, the measurement precision improves linearly with atom number N. The latter could probably be increased in the future by means of optimized loading protocols, such as a recooling and retrapping sequence, in the two-dimensional optical lattice.

It is known that, in the presence of noise, HS reverts back to a fixed improvement over the SQL (that is, $N^{-1/2}$ scaling) at sufficiently large atom number[39,40]. In our system, in the full interferometer demonstrated in Fig. 4c, the expected dominant limitation is the finite vacuum that induces an atom loss rate of $\gamma_{\mathrm{loss}} = 0.1\,\mathrm{s}^{-1}$. The latter results in a transition from HS to SQL scaling at $N \approx 4 \times 10^4$ (Methods) for the Ramsey time of 3.46 ms used here. This is larger than the maximum

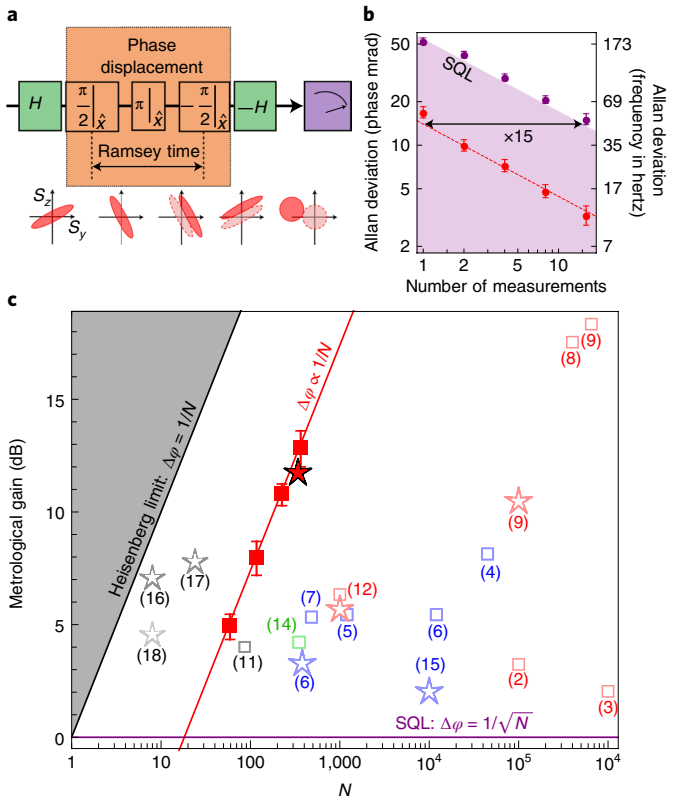

Fig. 4 | The scaling of the sensitivity with the atom number and a comparison with previous results. a, A block diagram showing a SATIN scheme applied to a Ramsey interferometry experiment, that is, the compound sequence of pulses that maps the phase accumulated during the Ramsey time into a phase displacement about the S_y axis. The purple box denotes the final state read-out. The state at different moments of the protocol is represented by the cartoons below the block digram. **b**, A phase Allan deviation plot of Ramsey spin echo interferometry performed with a CSS (purple circles) and an optimally over-squeezed state in a SATIN protocol (red circles). In both cases, we used 340 ± 20 atoms in the interferometer. The shaded purple area indicates the region below the SQL. The data for the SATIN sequence are fitted to a white noise model (red dashed line) showing 11.8 ± 0.5 dB of metrological gain over the SQL. **c**, A comparison with previous results including Bose-Einstein Condensates experiments (blue)[4–7,15], thermal atoms (red)[2,3,8,9,12], ions (dark grey)[11,16,17] and Rydberg atoms in a tweezer array (light grey)[18]. The green point shows the squeezing generated in an optical lattice clock[14]. Squares show expected metrological gains obtained by quantum state characterization. Stars indicate directly measured phase sensitivity gains. Solid symbols are obtained in this work. Error bars represent 1σ confidence intervals. The horizontal error bars are smaller than the markers.

atom number (10^2–10^4) used in optical-transition clocks to keep systematic errors through collisional shifts under control[38]. However, to retain HS to this level, technical parameters, such as the squeezing light and the radiofrequency (RF) rotation pulses, need to be stringently controlled. Furthermore, the relative photon number of the $\tilde{Q}_+/\tilde{Q}_-$ shearing/unshearing pulses must be stable near the shot noise level, which corresponds to a moderate 5% for our ensemble size.

Our protocol can be used for a variety of fundamental and applied purposes, such as tests of fundamental laws of physics[41,42], the search for physics beyond the Standard Model[43–46], the detection of gravitational waves[47] or geodesy[48,49]. As with all entanglement-based protocols beyond the SQL, it is useful to boost the sensitivity in applications that require performance in a given bandwidth or limited time. For instance, by coherently transferring the entanglement onto the ultra-narrow optical clock transition by means of a high-fidelity optical π pulse[14,50], the protocol can be used directly to search for transient changes in the fundamental constants induced by dark matter[43].

Online content

Any methods, additional references, Nature Research reporting summaries, source data, extended data, supplementary information, acknowledgements, peer review information; details of author contributions and competing interests; and statements of data and code availability are available at https://doi.org/10.1038/s41567-022-01653-5.

Received: 13 October 2021; Accepted: 26 May 2022;
Published online: 14 July 2022

References

1. Takano, T., Fuyama, M., Namiki, R. & Takahashi, Y. Spin squeezing of a cold atomic ensemble with the nuclear spin of one-half. *Phys. Rev. Lett.* **102**, 033601 (2009).
2. Appel, J. et al. Mesoscopic atomic entanglement for precision measurements beyond the standard quantum limit. *Proc. Natl Acad. Sci. U. S. A.* **106**, 10960–10965 (2009).
3. Sewell, R. J. et al. Magnetic sensitivity beyond the projection noise limit by spin squeezing. *Phys. Rev. Lett.* **109**, 253605 (2012).
4. Hamley, C. D., Gerving, C., Hoang, T., Bookjans, E. & Chapman, M. S. Spin-nematic squeezed vacuum in a quantum gas. *Nat. Phys.* **8**, 305–308 (2012).
5. Berrada, T. et al. Integrated Mach–Zehnder interferometer for Bose–Einstein condensates. *Nat. Commun.* **4**, 1–8 (2013).
6. Muessel, W., Strobel, H., Linnemann, D., Hume, D. B. & Oberthaler, M. K. Scalable spin squeezing for quantum-enhanced magnetometry with Bose–Einstein condensates. *Phys. Rev. Lett.* **113**, 103004 (2014).
7. Schmied, R. et al. Bell correlations in a Bose–Einstein condensate. *Science* **352**, 441–444 (2016).
8. Cox, K. C., Greve, G. P., Weiner, J. M. & Thompson, J. K. Deterministic squeezed states with collective measurements and feedback. *Phys. Rev. Lett.* **116**, 093602 (2016).
9. Hosten, O., Engelsen, N. J., Krishnakumar, R. & Kasevich, M. A. Measurement noise 100 times lower than the quantum-projection limit using entangled atoms. *Nature* **529**, 505–508 (2016).
10. Hosten, O., Krishnakumar, R., Engelsen, N. J. & Kasevich, M. A. Quantum phase magnification. *Science* **352**, 1552–1555 (2016).
11. Bohnet, J. G. et al. Quantum spin dynamics and entanglement generation with hundreds of trapped ions. *Science* **352**, 1297 (2016).
12. Braverman, B. et al. Near-unitary spin squeezing in ^{171}Yb. *Phys. Rev. Lett.* **122**, 223203 (2019).
13. Bao, H. et al. Spin squeezing of 10^{11} atoms by prediction and retrodiction measurements. *Nature* **581**, 159–163 (2020).
14. Pedrozo-Peñafiel, E. et al. Entanglement on an optical atomic-clock transition. *Nature* **588**, 414–418 (2020).
15. Kruse, I. et al. Improvement of an atomic clock using squeezed vacuum. *Phys. Rev. Lett.* **117**, 143004 (2016).
16. Monz, T. et al. 14-qubit entanglement: creation and coherence. *Phys. Rev. Lett.* **106**, 130506 (2011).
17. Pogorelov, I. et al. Compact ion-trap quantum computing demonstrator. *PRX Quantum* **2**, 020343 (2021).
18. Omran, A. et al. Generation and manipulation of Schrödinger cat states in Rydberg atom arrays. *Science* **365**, 570–574 (2019).
19. Yurke, B., McCall, S. L. & Klauder, J. R. SU(2) and SU(1,1) interferometers. *Phys. Rev. A* **33**, 4033–4054 (1986).
20. Kitagawa, M. & Ueda, M. Squeezed spin states. *Phys. Rev. A* **47**, 5138–5143 (1993).
21. Wineland, D. J., Bollinger, J. J., Itano, W. M. & Heinzen, D. J. Squeezed atomic states and projection noise in spectroscopy. *Phys. Rev. A* **50**, 67–88 (1994).
22. Bollinger, J. J., Itano, W. M., Wineland, D. J. & Heinzen, D. J. Optimal frequency measurements with maximally correlated states. *Phys. Rev. A* **54**, R4649 (1996).
23. Pezzè, L., Smerzi, A., Oberthaler, M. K., Schmied, R. & Treutlein, P. Quantum metrology with nonclassical states of atomic ensembles. *Rev. Mod. Phys.* **90**, 035005 (2018).
24. Leibfried, D. et al. Creation of a six-atom 'Schrödinger cat' state. *Nature* **438**, 639–642 (2005).
25. Saffman, M., Oblak, D., Appel, J. & Polzik, E. S. Spin squeezing of atomic ensembles by multicolor quantum nondemolition measurements. *Phys. Rev. A* **79**, 023831 (2009).

26. Davis, E., Bentsen, G. & Schleier-Smith, M. Approaching the Heisenberg limit without single-particle detection. *Phys. Rev. Lett.* **116**, 053601 (2016).
27. Fröwis, F., Sekatski, P. & Dür, W. Detecting large quantum Fisher information with finite measurement precision. *Phys. Rev. Lett.* **116**, 090801 (2016).
28. Leibfried, D. et al. Toward Heisenberg-limited spectroscopy with multiparticle entangled states. *Science* **304**, 1476–1478 (2004).
29. Toscano, F., Dalvit, D. A. R., Davidovich, L. & Zurek, W. H. Sub-Planck phase-space structures and Heisenberg-limited measurements. *Phys. Rev. A* **73**, 023803 (2006).
30. Nolan, S. P., Szigeti, S. S. & Haine, S. A. Optimal and robust quantum metrology using interaction-based readouts. *Phys. Rev. Lett.* **119**, 193601 (2017).
31. Macrì, T., Smerzi, A. & Pezzè, L. Loschmidt echo for quantum metrology. *Phys. Rev. A* **94**, 010102 (2016).
32. Strobel, H. et al. Fisher information and entanglement of non-Gaussian spin states. *Science* **345**, 424–427 (2014).
33. Lücke, B. et al. Twin matter waves for interferometry beyond the classical limit. *Science* **334**, 773–776 (2016).
34. Barontini, G., Hohmann, L., Haas, F., Estève, J. & Reichel, J. Deterministic generation of multiparticle entanglement by quantum Zeno dynamics. *Science* **349**, 1317–1321 (2015).
35. Linnemann, D. et al. Quantum-enhanced sensing based on time reversal of nonlinear dynamics. *Phys. Rev. Lett.* **117**, 013001 (2016).
36. Gilmore, K. A. et al. Quantum-enhanced sensing of displacements and electric fields with two-dimensional trapped-ion crystals. *Science* **373**, 673–678 (2021).
37. Bohnet, J. G. et al. Reduced spin measurement back-action for a phase sensitivity ten times beyond the standard quantum limit. *Nat. Photonics* **8**, 731–736 (2014).
38. Nicholson, T. et al. Systematic evaluation of an atomic clock at 2×10^{-18} total uncertainty. *Nat. Commun.* **6**, 6896 (2015).
39. Escher, B., de Matos Filho, R. & Davidovich, L. General framework for estimating the ultimate precision limit in noisy quantum-enhanced metrology. *Nat. Phys.* **7**, 406–411 (2011).
40. Demkowicz-Dobrzański, R., Kołodyński, J. & Guţă, M. The elusive Heisenberg limit in quantum-enhanced metrology. *Nat. Commun.* **3**, 1063 (2012).
41. Safronova, M. S. et al. Search for new physics with atoms and molecules. *Rev. Mod. Phys.* **90**, 025008 (2018).
42. Safronova, M. S. The search for variation of fundamental constants with clocks. *Ann. Phys.* **531**, 1800364 (2019).
43. Derevianko, A. & Pospelov, M. Hunting for topological dark matter with atomic clocks. *Nat. Phys.* **10**, 933–936 (2014).
44. Arvanitaki, A., Huang, J. & Van Tilburg, K. Searching for dilaton dark matter with atomic clocks. *Phys. Rev. D* **91**, 015015 (2015).
45. Wcislo, P. et al. New bounds on dark matter coupling from a global network of optical atomic clocks. *Sci. Adv.* **4**, eaau4869 (2018).
46. Stadnik, Y. & Flambaum, V. Axion-induced effects in atoms, molecules, and nuclei: parity nonconservation, anapole moments, electric dipole moments, and spin-gravity and spin-axion momentum couplings. *Phys. Rev. D* **89**, 043522 (2014).
47. Kolkowitz, S. et al. Gravitational wave detection with optical lattice atomic clocks. *Phys. Rev. D* **94**, 124043 (2016).
48. Grotti, J. et al. Geodesy and metrology with a transportable optical clock. *Nat. Phys.* **14**, 437–441 (2018).
49. Takamoto, M. et al. Test of general relativity by a pair of transportable optical lattice clocks. *Nat. Photonics* **14**, 411–415 (2020).
50. Young, A. W. et al. Half-minute-scale atomic coherence and high relative stability in a tweezer clock. *Nature* **588**, 408–413 (2020).

Publisher's note Springer Nature remains neutral with regard to jurisdictional claims in published maps and institutional affiliations.

© The Author(s), under exclusive licence to Springer Nature Limited 2022

Methods

Atom loading and cooling. We load ^{171}Yb atoms, which have purely nuclear spin of −1/2 in the ground state, into a two-colour mirror magneto-optical trap (MOT)[51] on the singlet $^1S_0 \rightarrow {}^1P_1$ and triplet $^1S_0 \rightarrow {}^3P_1$ transitions, followed by a second-stage green MOT on the triplet transition[51]. By changing the magnetic field, the atomic cloud is then transported into the intersection region of the cavity TEM_{00} mode and a one-dimensional optical lattice along the x direction. This transport is necessary because the geometrical centre of the MOT coils does not coincide with the cavity axis. Reference [52] gives the experimental details of the transfer of the atoms from the MOT to the optical lattice. The trap is formed by 'magic-wavelength' light with $\lambda_t \approx 759$ nm, and the trap depth is $U_x = k_B \times 10\,\mu K$. The green MOT light is then turned off, and the magic-wavelength trap inside the cavity, detuned from the x lattice by 160 MHz to avoid interference, is ramped up in 40 ms to a trap depth of the cavity lattice of $U_c = k_B \times 120\,\mu K$. At the end of the loading process, the transverse lattice power is ramped down to zero and back to full power in 50 ms to remove all the atoms that are outside the overlap region of the two lattices. In this way, an ensemble of atoms is prepared at a distance of 180 μm from the end mirror of the cavity, where the single-atom peak cooperativity is $\eta = 7.7 \pm 0.3$.

After loading, Raman sideband cooling is performed on the transition $^1S_0 \rightarrow {}^3P_1$ in an applied magnetic field of $B_z = 13.6$ G along the z direction. In 100 ms, the atomic temperature is lowered to ~2 μK, corresponding to an average motional occupation number of $\langle n_x \rangle = 0.2$ at a trap vibration frequency of $\omega_x/(2\pi) = 67$ kHz along the x direction. The cavity trap is then adiabatically ramped down to $U_c = k_B \times 40\,\mu K$ to further reduce the temperature. This corresponds to a trap frequency in the cavity direction of $\omega_z/(2\pi) = 90$ kHz. The temperature in the direction of the cavity axis is ~2 μK, resulting in an average motional occupation number of $\langle n_z \rangle = 0.1$. The cavity lattice has a waist of 9 μm, while the transverse lattice has a waist of 27 μm. The atomic cloud is confined in the intersection of these two beams and has r.m.s. sizes of 12 μm along the cavity axis ($\hat{z}$) and 3 μm along the transverse ($\hat{x}$) direction[53]. We observe that, during the Raman sideband cooling, where the optical pumping is provided by intracavity light, the atoms reorganize along the lattice such that all atoms have nearly the maximum coupling η to the cavity mode and the squeezing light[14,52,54]. Previously, this has been achieved with a wavelength of the trapping light that was twice the probing wavelength[55]. Here, contemplating applications on the optical clock transition[14], our trap is at a magic wavelength for the clock transition.

Initialization of the experimental sequence. After performing Raman sideband cooling that leaves the atoms spin polarized in the state $|\uparrow\rangle = |m_I = +1/2\rangle$, the ensemble is prepared into a CSS of the two magnetic sublevels of the ground state $|^1S_0\rangle$ ($|m_I = \pm 1/2\rangle$). We drive this transition by using RF pulses generated by a pair of coils in the presence of an external magnetic field of $B_z = 13.6$ G, corresponding to a Larmor frequency of $2\pi \times 10.2$ kHz. The Rabi frequency of the RF pulses is $2\pi \times 208(2)$ Hz. After the CSS is prepared, the SATIN protocol starts. Extended Data Fig. 1 shows the three experimental stages of our protocol.

State measurement. The single measurement outcome of $\hat{S}_z$ is obtained from the difference $S_z = (N_\uparrow - N_\downarrow)/2$ between the populations $N_\uparrow$ and $N_\downarrow$ of the states $|\uparrow\rangle$ and $|\downarrow\rangle$, respectively. We first measure $N_\uparrow$ through the vacuum Rabi splitting of the cavity mode $2g \approx \sqrt{N_\uparrow \eta \kappa \Gamma}$ when the empty cavity is resonant with the transition $|\uparrow\rangle \rightarrow |e\rangle = |^3P_1, m_F = +3/2\rangle$ (ref. [12]). Here, $\kappa = 2\pi \times 530(10)$ kHz is the cavity linewidth and $\Gamma = 2\pi \times 184(1)$ kHz the linewidth of the atomic transition. The Rabi splitting is measured by scanning the laser frequency and detecting the cavity transmission as a function of the frequency. To measure $N_\downarrow$, we swap the population between the $|\uparrow\rangle$ and $|\downarrow\rangle$ states through the application of an RF π pulse about the S_x axis and repeating the measurement procedure described above. The sum $N_\uparrow + N_\downarrow$ gives the total atom number N in one experimental shot.

The resolution of a single measurement, normalized to the SQL, is given by $\sigma^2_{meas} = \frac{1}{S_0} \mathrm{var}(S_{z1} - S_{z2})$ where S_{z1} and S_{z2} are two state measurements performed after a single CSS preparation. We obtain $\sigma^2_{meas} = 0.15 \pm 0.02$, and this remains constant within the whole range of atom numbers used in this experiment. Since all the atoms have the same coupling to the cavity, the atom number N inferred from the Rabi splitting equals the real number of atoms in the cavity.

For experiments requiring a measurement of $\hat{S}_y$, we apply an RF π/2 pulse about the x axis and then measure $\hat{S}_z$ as described above.

Single-atom cooperativity measurement. We can calculate the single-atom cooperativity η accurately from our cavity parameters[12,14,54]. With a measured finesse of $\mathcal{F} = 11{,}400$ and atoms loaded 0.246 ± 0.004 mm from the micromirror[54], we expect a single-atom cooperativity of $\eta = 7.8 \pm 0.2$.

We also verify this by measuring the spin projection noise via the cavity as a function of the collective cooperativity $N\eta$. For a CSS prepared at the equator of the generalized Bloch sphere, the measured variance of the difference ηS_z is

$$\mathrm{var}(\eta S_z) = (N\eta)\frac{\eta(1+\sigma_d^2)}{4}, \tag{3}$$

where we have also included the contribution due to the measurement noise σ^2_{meas}. The latter contribution is obtained through the variance of the difference between two measurements after a single CSS preparation.

Plotting the variance of ηS_z as a function of the collective cooperativity results, in the absence of classical sources of noise, in a linear graph with a slope of $\eta(1 + \sigma^2_{meas})/4$ (Extended Data Fig. 2). Since the measurement resolution normalized to the CSS spin projection noise $\sigma^2_{meas} = 0.15 \pm 0.02$ is a constant, we obtain a single-atom cooperativity of $\eta = 7.7 \pm 0.3$ by fitting the data to a linear model, in good agreement with our direct calculation from the measured cavity parameters. When a quadratic fitting term is included to account for possible technical noise, we recover the same cooperativity ($\eta = 7.7 \pm 0.9$) within error bars.

The single-atom cooperativity inferred form spin projection noise measurements agrees with the calculated one within error bars (Extended Data Fig. 2).

Cavity-induced one-axis twisting. The squeezing Hamiltonian is the result of the interaction of the atomic ensemble with the single-mode light inside the optical cavity, which is given by (equation (15) in ref. [56])

$$\begin{aligned}\hat{H}_{dip} &= -\left(\hat{S}_z + S_0\right)\eta\frac{|\hat{\mathcal{E}}_c|^2}{\omega}\frac{\pi}{\mathcal{F}}\mathcal{L}_d(x_a)\\ &= -\hbar\Omega\hat{n}_c\left(\hat{S}_z + S_0\right),\end{aligned} \tag{4}$$

where $\hat{\mathcal{E}}_c$ is the amplitude of the intracavity field, $\mathcal{F}$ is the cavity Finesse, $\mathcal{L}_d(x_a) = -\frac{x_a}{1+x_a^2}$ is the dispersive Lorentzian profile with $x_a \equiv 2\Delta/\Gamma$ the normalized detuning of the probe laser ω_l from the atomic resonance ω_a ($\Delta = \omega_l - \omega_a$) with respect to the natural linewidth of the transition (Γ). In this expression, $\Omega = \pi\eta\mathcal{L}_d(x_a)\kappa/\mathcal{F}$ represents the light shift per photon inside the cavity with κ the cavity linewidth, and $\hat{n}_c = |\hat{\mathcal{E}}_c|^2/(2\hbar\omega\kappa)$ the photon number inside the cavity. The second term of this Hamiltonian represents a global rotation that is cancelled by the spin echo sequence. This leads to a Hamiltonian $\hat{H} = -\hbar\Omega\hat{n}_c\hat{S}_z$ that depends on $\hat{S}_z$ and the number of photons inside the cavity.

When the CSS is close to the equator of the Bloch sphere, $\langle \hat{S}_z \rangle = 0$, we can expand the photon number $\hat{n}_c(\hat{S}_z)$ in terms of $\hat{S}_z$ and write the Hamiltonian as

$$\hat{H} = -\hbar\Omega\hat{S}_z\sum_{j=0}^{\infty}\frac{\hat{S}_z^j}{j!}\left(\frac{\partial^j\hat{n}_c}{\partial\hat{S}_z^j}\right)_{\langle\hat{S}_z\rangle=0}. \tag{5}$$

The zeroth-order term of this expansion ($\hat{H}_0 = -\hbar\Omega\langle\hat{n}_c\rangle\hat{S}_z$) represents a rotation of the collective state around the S_z axis of the Bloch sphere, which is also cancelled by the spin echo sequence. The first-order term of the expansion,

$$\hat{H}_1 = -\hbar\chi\hat{S}_z^2, \tag{6}$$

is the known one-axis twisting Hamiltonian[20]. This term represents the effective spin–spin interaction mediated by light and produces a rotation of the atomic spin around the S_z axis that is proportional to $\hat{S}_z$, producing the squeezed distribution of the collective atomic state (Extended Data Fig. 3). The twisting or shearing parameter is given by

$$\chi = -\eta\mathcal{L}_d(x_a)\left(1 - x_a + \frac{N}{2}\eta\right)\mathcal{T}_0\frac{\mathcal{S}}{N/2}, \tag{7}$$

which is proportional to the scattered photon number into free space $\mathcal{S}$. Here, $\mathcal{T}_0$ is the power transmitted through a symmetric and lossless cavity, given by

$$\mathcal{T}_0 = \frac{|\mathcal{E}_t|^2}{|\mathcal{E}_r|^2} = \frac{1}{\left(1 + \frac{N}{2}\eta\mathcal{L}_a(x_a)\right)^2 + \left(x_c + \frac{N}{2}\eta\mathcal{L}_d(x_a)\right)^2}, \tag{8}$$

and we have defined the dispersive and absorptive Lorentzian profiles $\mathcal{L}_d(x) = -\frac{x}{1+x^2}$, and $\mathcal{L}_a(x) = \frac{1}{1+x^2}$, respectively. $x_c \equiv 2\delta/\kappa$ is the detuning of the probe beam from the cavity resonance frequency ω_c ($\delta = \omega_l - \omega_c$) normalized to the cavity linewidth. Higher-order terms in the expansion of equation (5) are negligible (<1%) at our chosen detuning.

To implement the effective cavity-induced OAT Hamiltonian, equation (1), we first tune the frequency of the high-finesse cavity ω_c in resonance with the $|\uparrow\rangle \rightarrow |e\rangle = |^3P_1, m_F = +3/2\rangle$ transition at a frequency of ω_a, so that strong coupling of the cavity field to the atoms results in vacuum Rabi splitting (Fig. 1). A pulse of light with frequency ω_l tuned to the slope of a Rabi peak (Fig. 1) will pass through the cavity and interact with the atoms, resulting in the first-order phase shift $\beta\hat{S}_z$ and shearing $\chi\hat{S}_z^2$ (refs. [12,56]). After cancelling the first-order phase shift with a spin echo sequence[14], the system evolution can be described by the OAT Hamiltonian $\hat{H} = \chi\hat{S}_z^2$.

It is useful to express the action of the OAT Hamiltonian in terms of the normalized twisting parameter

$$\tilde{Q} \equiv \sqrt{N}\chi\tau, \tag{9}$$

where $\tilde{Q}$ is the r.m.s. angle subtended by the state on the Bloch sphere, and τ is the entangling time, that is, the action time of the OAT Hamiltonian. Using ref. [56], the twisting parameter can be expressed as

$$\tilde{Q} = \frac{n_{\mathrm{tr}}^{\mathrm{tot}}}{\sqrt{N}}\mathcal{L}_{\mathrm{d}}(x_{\mathrm{a}})\mathcal{L}_{\mathrm{a}}(x_{\mathrm{a}})\frac{\frac{N}{2}\eta^2(1+\frac{N}{2}\eta - x_{\mathrm{a}}x_{\mathrm{c}})}{\left(1+\frac{N}{2}\eta\mathcal{L}_{\mathrm{a}}(x_{\mathrm{a}})\right)^2+\left(x_{\mathrm{c}}+\frac{N}{2}\eta\mathcal{L}_{\mathrm{d}}(x_{\mathrm{a}})\right)^2}, \quad (10)$$

where $n_{\mathrm{tr}}^{\mathrm{tot}}$ is the total number of photons transmitted through the cavity.

We notice that $\tilde{Q}(-x_{\mathrm{a}}, -x_{\mathrm{c}}) = -\tilde{Q}(x_{\mathrm{a}}, x_{\mathrm{c}})$. This means that the sign of the shearing parameter (that is, the 'shearing direction') can be switched by changing the sign of the detuning of the laser frequency from the atomic (and cavity mode) transition frequency $\omega_{\mathrm{a}}=\omega_{\mathrm{c}}$. Hence, from equation (9), $\chi = \tilde{Q}/(\tau\sqrt{N})$, it follows that the sign of the Hamiltonian is also switched (Extended Data Fig. 4).

Similarly, we evaluate the additional light-induced broadening $\mathcal{I}$ of the phase noise of the atomic state. ($\mathcal{I} = 1$ means that the additional broadening equals the CSS variance.)

$$\mathcal{I} = 2\,n_{\mathrm{tr}}^{\mathrm{tot}}\mathcal{L}_{\mathrm{a}}^2(x_{\mathrm{a}})\frac{(N/2)\eta^2(1+N\eta/2+x_{\mathrm{a}}^2)}{\left(1+(N/2)\eta\mathcal{L}_{\mathrm{a}}(x_{\mathrm{a}})\right)^2+\left(x_{\mathrm{c}}+(N/2)\eta\mathcal{L}_{\mathrm{d}}(x_{\mathrm{a}})\right)^2}. \quad (11)$$

We also consider the effects on $\tilde{Q}$ and $\mathcal{I}$ of atoms populating the $|\downarrow\rangle$ level (see ref. [56] for details). Atoms in the $|\downarrow\rangle$ state have a similar contribution to the polarizability as atoms in $|\uparrow\rangle$, but the corresponding transition will be detuned due to the Zeeman shift $\Delta_Z \approx 20$ MHz between the excited sublevels $|^3P_1, m_{\mathrm{F}} = +1/2\rangle$ and $|\mathrm{e}\rangle = |^3P_1, m_{\mathrm{F}} = +3/2\rangle$, due to the 14 G magnetic field applied along the z axis (Fig. 1).

Quantum noise in S_y quadrature. We first consider the phase of the spin vector τ_y in the absence of contrast loss of the signal, defined as $\tau_y \equiv \sqrt{2|\langle\hat{\mathbf{S}}\rangle|}\arcsin\left(\langle\hat{S}_y\rangle/|\langle\hat{\mathbf{S}}\rangle|\right)$ for $\tau_y < \pi/2$.

After letting an initial CSS evolve forward and backward under the OAT Hamiltonian, the variance $\Delta\tau_y^2$ is

$$\Delta\tau_y^2 = \frac{1+\mathcal{I}_{\mathrm{tot}}}{2S_0} + \tilde{Q}_{\mathrm{tot}}^2, \quad (12)$$

where $\tilde{Q}_{\mathrm{tot}} = \tilde{Q}_+ + \tilde{Q}_-$ and $\mathcal{I}_{\mathrm{tot}} = \mathcal{I}_+ + \mathcal{I}_-$, that is, the sum of the excess broadenings induced by the twisting ($\mathcal{I}_+$) and untwisting ($\mathcal{I}_-$) procedures. This results in a spin variance normalized to the CSS of

$$\frac{2\mathrm{var}(S_y)}{S_0} \equiv \sigma_y^2 = \frac{1}{2} + \frac{1}{2}\exp\left(-2\Delta\tau_y^2\right). \quad (13)$$

Contrast loss. During the twisting and untwisting processes, there is contrast reduction or, equivalently, a shrinking of the radius of the Bloch sphere associated with the collective atomic spin. The reduction of the length of the spin vector owing to photon scattering is given by

$$\mathcal{C}_{\mathrm{sc}} \equiv \frac{\langle|\mathbf{S}|\rangle}{S_0} = \exp\left(-2\frac{n_{\mathrm{sc}}(\tilde{Q}_+, \tilde{Q}_-)}{N}\right), \quad (14)$$

where $n_{\mathrm{sc}}(\tilde{Q}_+, \tilde{Q}_-)$ is the total number of photons scattered into free space to generate both $\tilde{Q}_+$ and $\tilde{Q}_-$.

To evaluate the spin noise projection on the S_y quadrature, we first consider the spin phase noise of the coherent sub-ensemble of atoms, that is, of the atoms that have not scattered a photon into free space. The spin vector length of this sub-ensemble is $\langle|\mathbf{S}|\rangle$, and the resulting spin phase variance is

$$\Delta\tau_y^2 = \frac{1+\mathcal{I}_{\mathrm{tot}}}{2\mathcal{C}_{\mathrm{sc}}S_0} + \tilde{Q}_{\mathrm{tot}}^2. \quad (15)$$

It is worth noting that neither $\tilde{Q}_{\mathrm{tot}}$ nor $\mathcal{I}_{\mathrm{tot}}$ is affected by the contrast loss. They depend solely on the S_z projection, which here we can consider as being left unchanged by the entangling light.

Considering the spin variance contribution of the atoms that have scattered a photon and whose states are uncorrelated with the ensemble, we obtain a normalized spin variance of

$$\frac{\mathrm{var}(S_y)}{S_0/2} = 1 - \mathcal{C}_{\mathrm{sc}} + S_0\mathcal{C}_{\mathrm{sc}}^2\left\{1 - \exp\left[-2\left(\frac{1+\mathcal{I}_{\mathrm{tot}}}{2\mathcal{C}_{\mathrm{sc}}S_0} + \tilde{Q}_{\mathrm{tot}}^2\right)\right]\right\}. \quad (16)$$

Under the Holstein–Primakoff approximation ($\mathcal{I} \ll N$, $\tilde{Q} \ll 1$), the variance of the state reduces to

$$\frac{\mathrm{var}(S_y)}{S_0/2} = 1 + 2S_0\mathcal{C}_{\mathrm{sc}}^2\,\tilde{Q}_{\mathrm{tot}}^2 + \mathcal{C}_{\mathrm{sc}}\mathcal{I}_{\mathrm{tot}}. \quad (17)$$

Signal amplification. The expression for the signal amplification as a function of the twisting strength is derived in ref. [26] and for $N \gg 1$ reads

$$m(\tilde{Q}) \approx \mathcal{C}_{\mathrm{sc}}(\tilde{Q}) \times (N-1)\sin\left(\frac{\tilde{Q}}{\sqrt{N}}\right)\cos^{N-2}\left(\frac{\tilde{Q}}{\sqrt{N}}\right), \quad (18)$$

where $\tilde{Q} = \tilde{Q}_+ = \tilde{Q}_-$. Note that, for small $\tilde{Q} \ll 1$, the maximal signal enhancement is obtained when the state is displaced not along S_y but at an angle $\theta \approx \arctan(1/m)$ to it, or for an optimized $\tilde{Q}_- > \tilde{Q}_+$ (ref. [57]). However, here we are interested in $\tilde{Q} \approx 1$, where $\theta \approx 0$, and we induce or measure displacements directly along the S_y axis.

Light shift during OAT. During the OAT process, the zeroth-order term of the Hamiltonian in equation (5) induces an absolute light shift of $\phi_{\mathrm{lightshift}} \approx 8\,\pi \times \tilde{Q}$. This contribution is cancelled by a spin echo sequence[12].

The light shift is induced by the average number of photons n_{avg} transmitted through the cavity. Under optimized detuning, for every atom number N, the average photon number is given by $n_{\mathrm{avg}} \approx 1.6 \times N \times \tilde{Q}$.

Limitation to the HS. Following the framework established in refs. [39,40], we evaluate the bounds on the metrological gain for our SATIN protocol applied to state-of-the-art optical lattice clocks. In particular, we assess the optimal constant metrological gain that can be asymptotically reached (taking into account the system noise) and the atom number where the transition from HS to SQL scaling is expected.

We use as a reference the parameters from the recent optical clock realization by Young et al.[50]. For optimized operating conditions, they report a measured atom–atom dephasing rate of $\gamma_{\mathrm{deph}} = 0.025\,\mathrm{s}^{-1}$, an atom loss rate of $\gamma_{\mathrm{loss}} = 0.01\,\mathrm{s}^{-1}$ and a spontaneous emission loss rate of $\gamma_{\mathrm{em}} = 0.01\,\mathrm{s}^{-1}$. It is worth noting that, in ref. [50], the average total atom number is $N = 150$, similar to our atom number. Extended Data Fig. 7 shows the expected metrological gain attainable with our SATIN protocol when applied to the optical clock realization of Young et al. as a function of the loaded atom number for two exemplary Ramsey times of $\tau = 50$ ms (red) and $\tau = 1$ s (blue). For the longer Ramsey time of 1 s, the SATIN protocol will nearly saturate the bound on the metrological gain for $N \geq 300$, that is, the regime studied in this work. For a much shorter Ramsey time of $\tau = 50$ ms ($\tau = 1$ ms), the transition between HS to SQL scaling occurs at $N \approx 5 \times 10^3$ ($N \approx 2.5 \times 10^5$). Note that many proposed applications[41–45,58], including gravitational wave detection[47], require a large bandwidth, that is, a short Ramsey time.

Computation of Wigner quasi-probability distribution functions. We compute the Wigner quasi-probability distributions on the Bloch sphere by following the efficient computation methods presented in ref. [59].

Data availability

The datasets generated and analysed during this study are available from the corresponding authors upon reasonable request. Source data are provided with this paper.

References

51. Kawasaki, A., Braverman, B., Yu, Q. & Vuletić, V. Two-color magneto-optical trap with small magnetic field for ytterbium. *J. Phys. B* **48**, 155302 (2015).
52. Kawasaki, A. et al. Trapping ^{171}Yb atoms into a one-dimensional optical lattice with a small waist. *Phys. Rev. A* **102**, 013114 (2020).
53. Hu, J. et al. Creation of a Bose-condensed gas of ^{87}Rb by laser cooling. *Science* **358**, 1078–1080 (2017).
54. Kawasaki, A. et al. Geometrically asymmetric optical cavity for strong atom–photon coupling. *Phys. Rev. A* **99**, 013437 (2019).
55. Lee, J., Vrijsen, G., Teper, I., Hosten, O. & Kasevich, M. A. Many-atom–cavity QED system with homogeneous atom–cavity coupling. *Opt. Lett.* **39**, 4005–4008 (2014).
56. Li, Z. et al. Collective spin-light and light-mediated spin-spin interactions in an optical cavity. *Phys. Rev. X Quantum* **3**, 020308 (2022).
57. Schulte, M., Martínez-Lahuerta, V. J., Scharnagl, M. S. & Hammerer, K. Ramsey interferometry with generalized one-axis twisting echoes. *Quantum* **4**, 268 (2020).
58. Pospelov, M. et al. Detecting domain walls of axionlike models using terrestrial experiments. *Phys. Rev. Lett.* **110**, 021803 (2013).
59. Koczor, B., Zeier, R. & Glaser, S. J. Fast computation of spherical phase-space functions of quantum many-body states. *Phys. Rev. A* **102**, 062421 (2020).

Acknowledgements

We thank B. Braverman, A. Kawasaki, M. Lukin and J. Ye for discussions. This work was supported by the NSF (grant no. PHY-1806765), DARPA (grant no. D18AC00037), ONR (grant no. N00014-20-1-2428), the NSF Center for Ultracold Atoms (CUA) (grant no. PHY-1734011) and NSF QLCI-CI QSEnSE (grant no. 2016244). S.C. and A.F.A. acknowledge support from the Swiss National Science Foundation (SNSF).

Author contributions

S.C., E.P.-P., A.F.A. and Z.L. led the experimental efforts and simulations. S.C., E.P.-P., A.F.A. and Z.L. contributed to the data analysis. V.V. conceived and supervised the experiment. S.C., E.P.-P., A.F.A. and V.V. wrote the manuscript. All authors discussed the experimental implementation and the results, and contributed to the manuscript.

Competing interests

The authors declare no competing interests.

Additional information

Extended data is available for this paper at https://doi.org/10.1038/s41567-022-01653-5.

Supplementary information The online version contains supplementary material available at https://doi.org/10.1038/s41567-022-01653-5.

Correspondence and requests for materials should be addressed to Vladan Vuletić.

Peer review information *Nature Physics* thanks Rafal Demkowicz-Dobrzansk and the other, anonymous, reviewer(s) for their contribution to the peer review of this work.

Reprints and permissions information is available at www.nature.com/reprints.

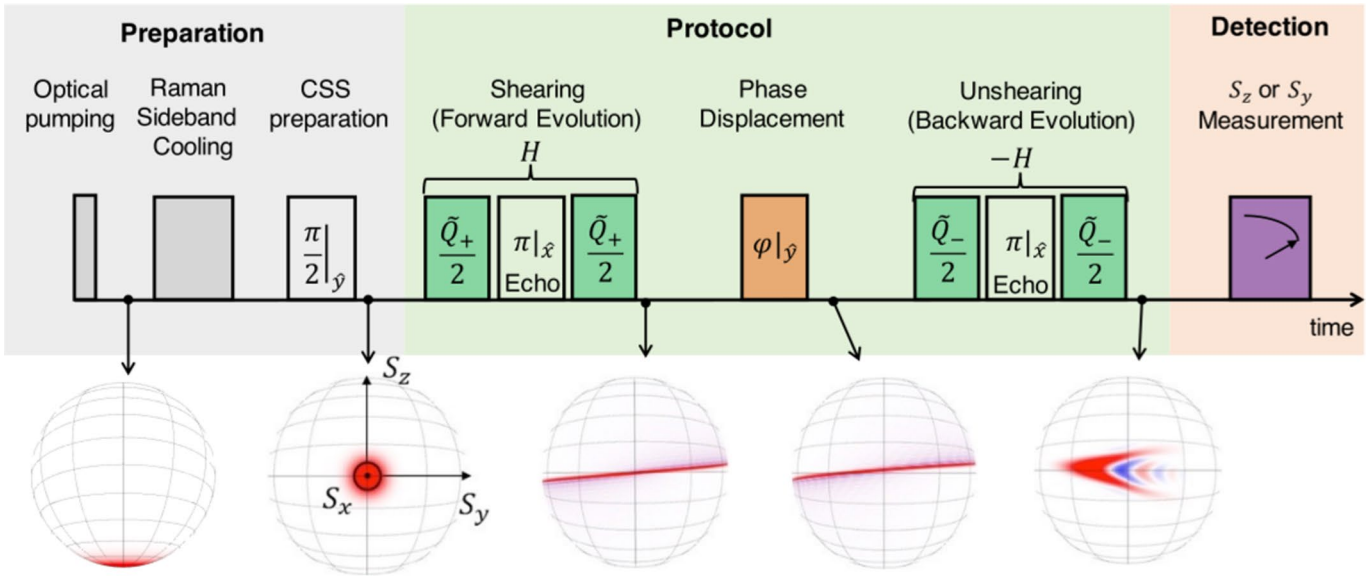

Extended Data Fig. 1 | Experimental sequence. The three stages of the experiment are represented in different color-shaded areas in the upper part: preparation, protocol, and detection. Bloch spheres (bottom) show the collective atomic state after the indicated process has been performed in time. The time axis is not to scale.

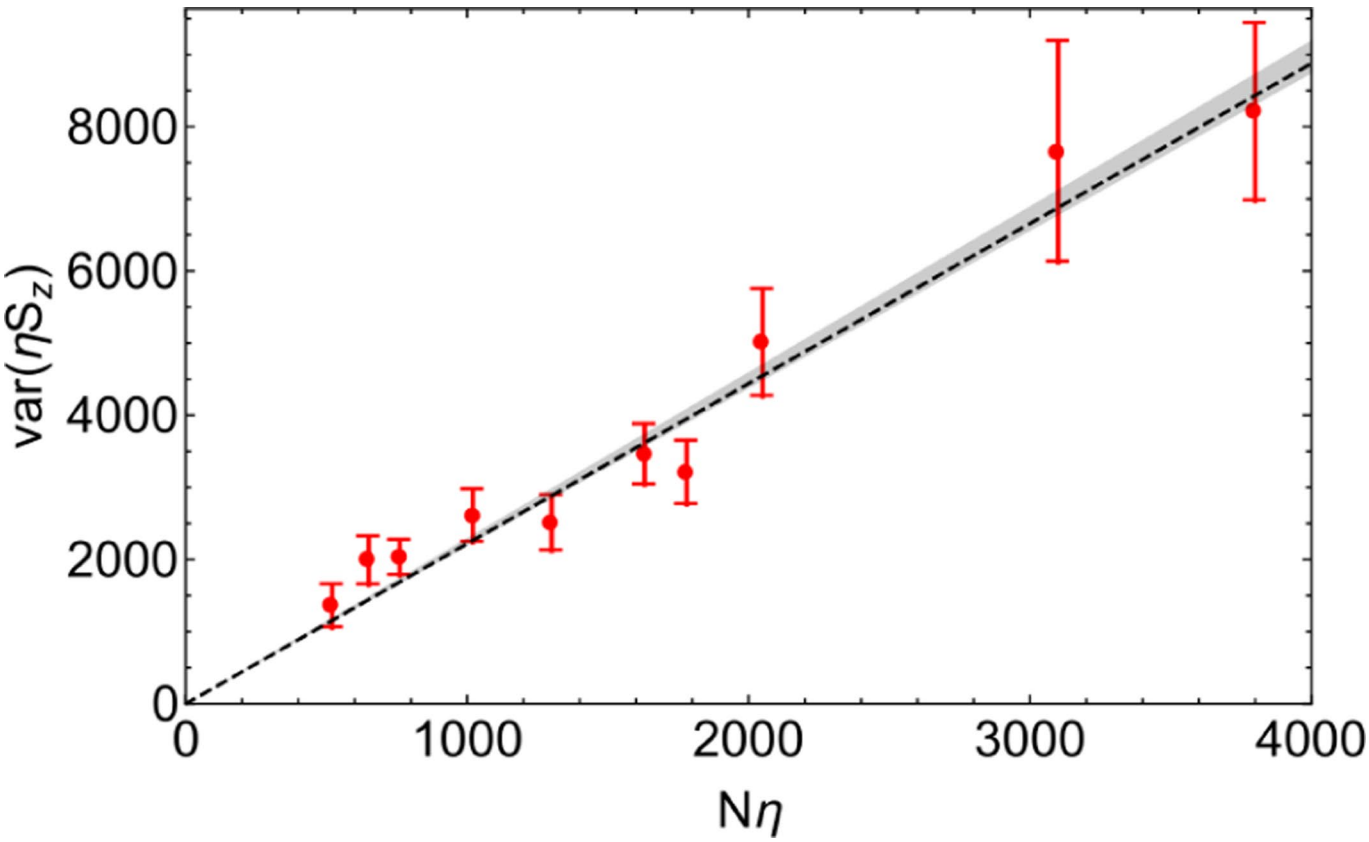

Extended Data Fig. 2 | Single-atom cooperativity. The dashed line represents the quadratic regression fit, with the prefactor of the linear term yielding the slope $\eta(1+\sigma^2_{\mathrm{meas}})/4 = 2.2 \pm 0.1$ and the quadratic term prefactor being consistent with zero $(0 \pm 3) \times 10^{-4}$. The gray band denotes the expected projection noise given by the single-atom cooperativity calculated from our cavity parameters $\eta = 7.8 \pm 0.2$. The linearity of the data indicates the classical sources of noise are negligible in the CSS state preparation, since they would manifest as a quadratic dependence of the measured variance on collective cooperativity $N\eta$. Each data point corresponds to the mean value obtained from 50 to 150 experimental realizations. The error bars correspond to 1 σ and are the standard error of a Gaussian distribution: $\sigma_s^2/(n-1)$, where σ_s is the sample variance and n is the number of experimental realizations. Statistical horizontal error bars are smaller than the marker size.

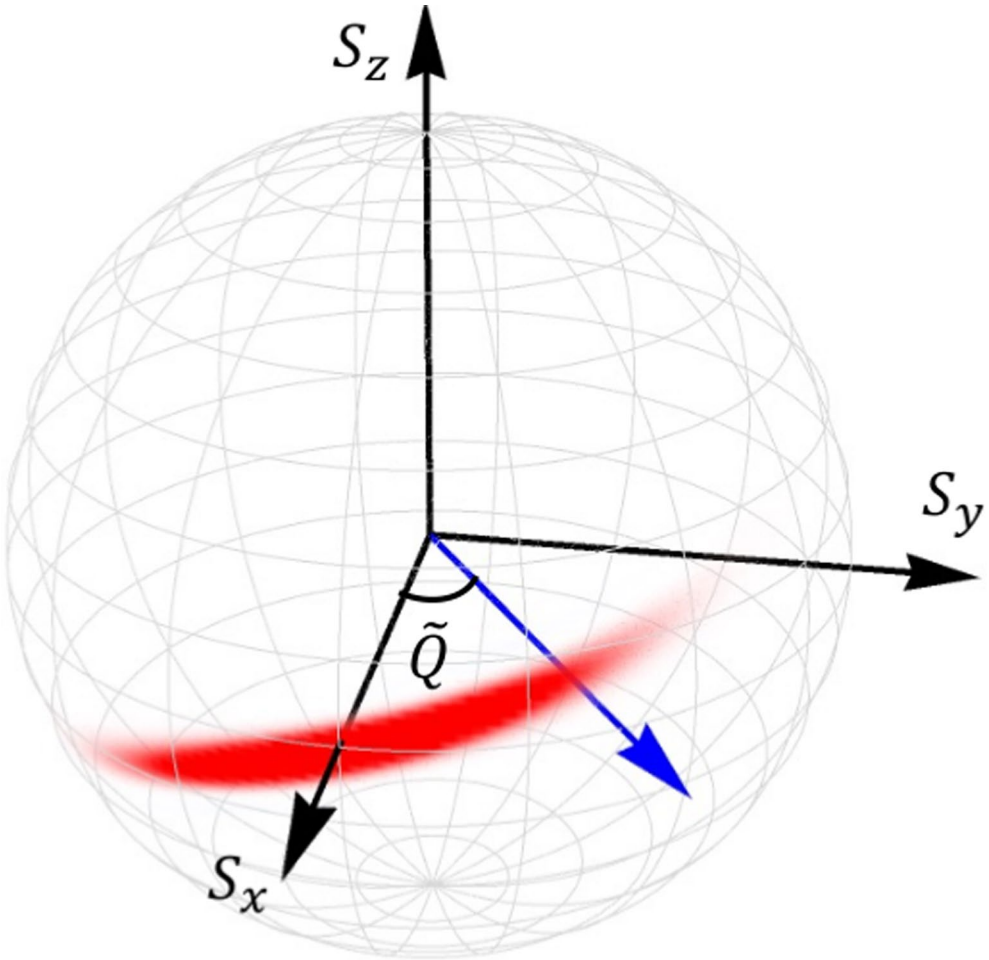

Extended Data Fig. 3 | Squeezed spin distribution on the generalized Bloch sphere. The normalized shearing strength $\tilde{Q}$ represents the angle subtended by the sheared distribution with respect to the *x*-axis, along which the initial CSS was prepared.

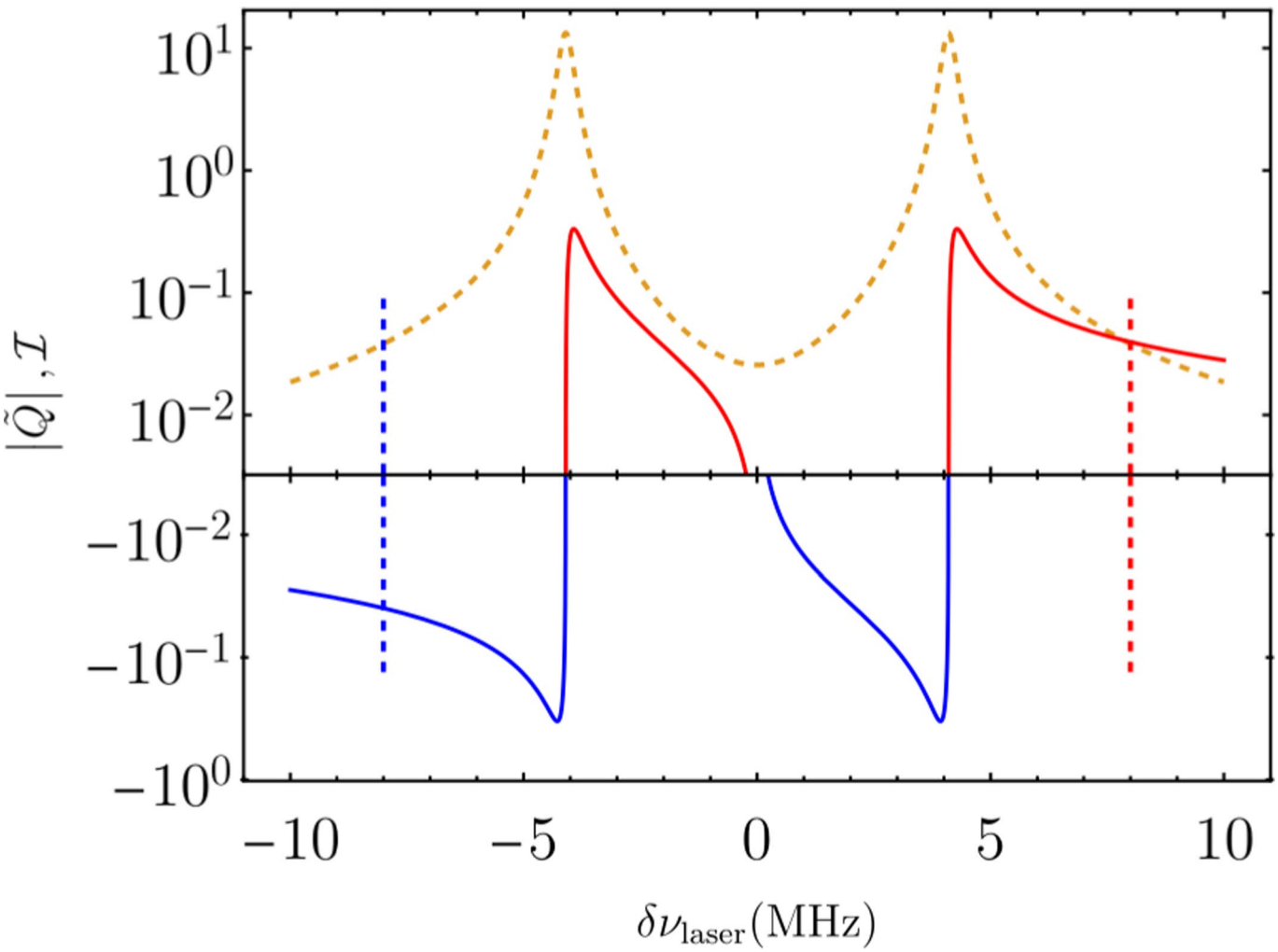

Extended Data Fig. 4 | Relevant parameters for our squeezing protocol. Excess broadening $\mathcal{I}$ (yellow dashed line) per scattered photon and shearing strength $|\tilde{Q}|$ (solid line). The red and blue parts of the solid line represent positive and negative values of $\tilde{Q}$, respectively, which lead to forward and backward evolution in time. The blue and red dashed lines represent the detuning, − 8 MHz and 8 MHz, chosen to generate $\tilde{Q}_+$ and $\tilde{Q}_-$, respectively. The duration of the entangling/disentangling pulses is about 4 ms. In this figure, we have used the experimental parameters $N = 220$ and $\eta = 7.7$. For illustration purposes, contrast loss has not been included.

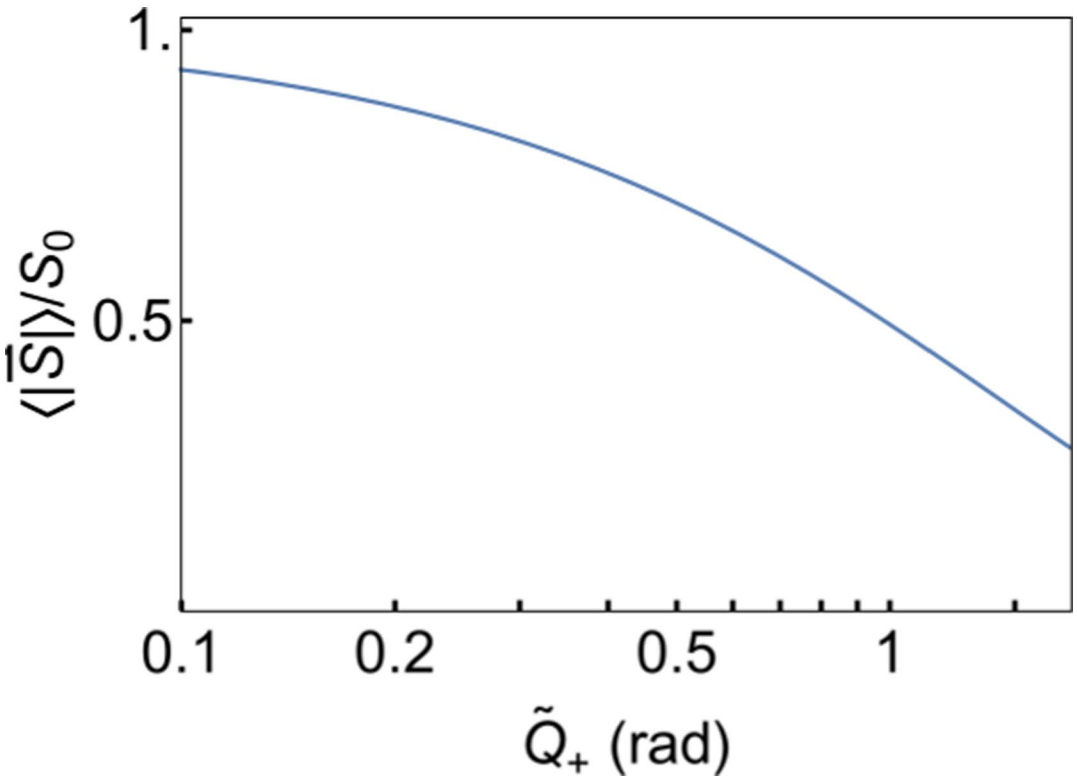

Extended Data Fig. 5 | SATIN contrast loss. Contrast reduction in an optimized SATIN protocol as a function of the twisting strength $\tilde{Q}_+$. "Optimized SATIN" means that the entangling light detuning is chosen in order to maximize the protocol's metrological gain. It is worth noting that, under this optimization condition, the contrast reduction is independent of the atom number.

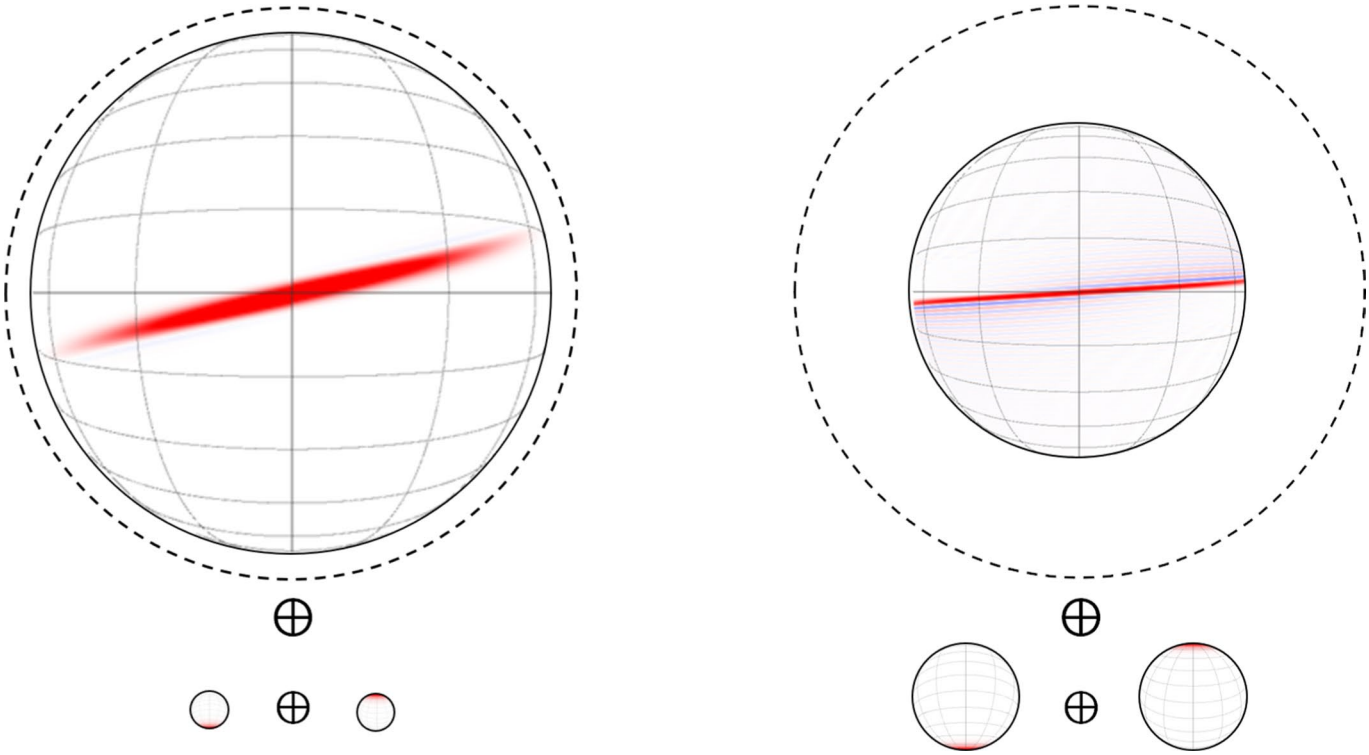

Extended Data Fig. 6 | Graphical representation of the model used to describe contrast loss due to scattering of photons into free space. The atomic spin can be decomposed into the coherent signal (large Bloch sphere) and the signals of the sub-ensembles of atoms that due to photon scattering have been projected into the spin states $|\uparrow\rangle$ or $|\downarrow\rangle$, and that have lost any coherence. The radii of the generalized Bloch-spheres represent the relative populations of the states. The dashed circle indicates the size of the generalized Bloch sphere size with all spin being in the same pure state, i.e., in the absence of contrast losses. The **left** figure corresponds to $\tilde{Q}_+ = 0.3$ (mostly Gaussian distribution) while the **right** figure is calculated for $\tilde{Q}_+ = 1.3$.

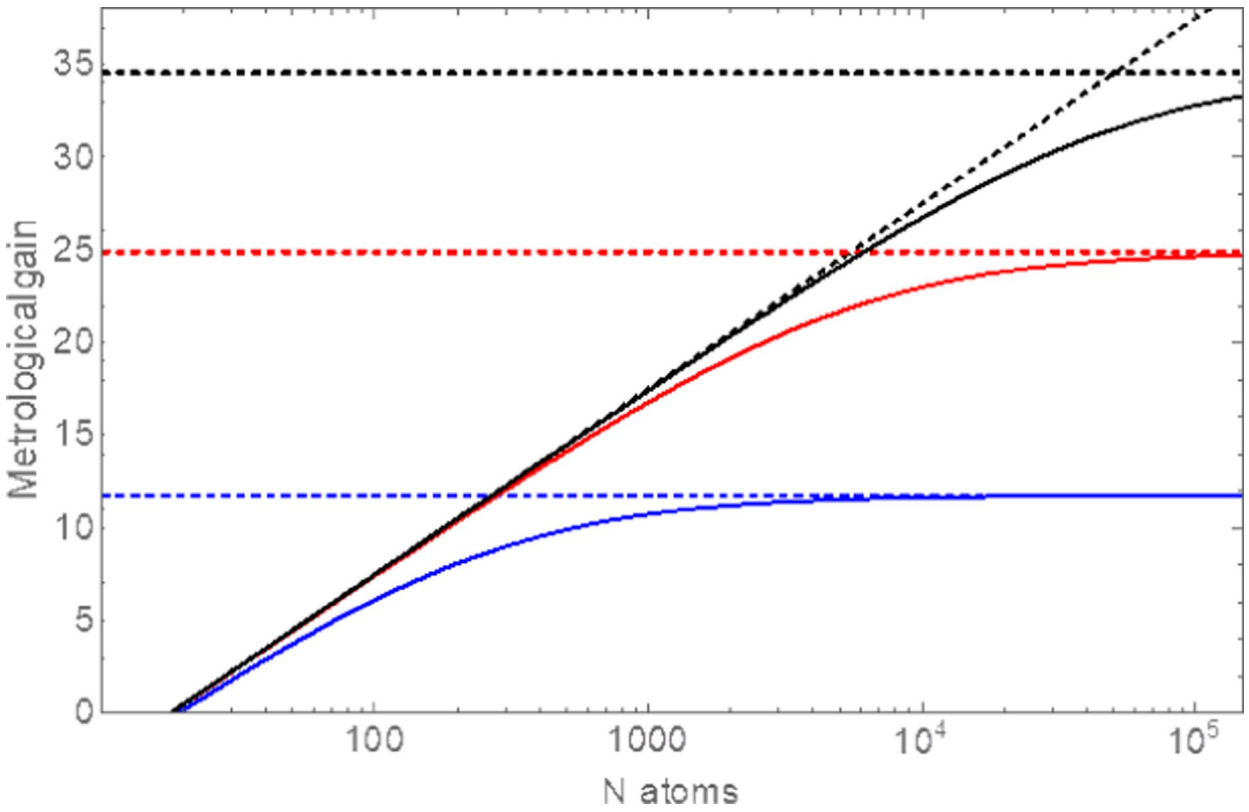

Extended Data Fig. 7 | Expected Metrological Gain in Optical Clocks. Dashed lines represent fundamental quantum limits. Solid lines represent metrological gain versus atom number expected in our system with a short Ramsey time of 3.5 ms (black) and an atom loss rate of $0.1s^{-1}$., and in a state-of-the-art optical clock operated with a SATIN protocol for Ramsey times of 50 ms (red) and 1 s (blue). We notice that the transition between HS to SQL scaling occurs in the region of $N = 4 \times 10^4$ and $N = 300$, respectively.